# Hierarchical radioscopy using polychromatic and partially coherent hard synchrotron radiation - revision 1

**Alexander Rack,[1] Francisco García-Moreno,[2,3] Lukas Helfen,[1,4] Manas Mukherjee,[2,3,5] Catalina Jiménez,[2,3] Tatjana Rack,[6] Peter Cloetens,[1] and John Banhart[2,3]**

[1]*European Synchrotron Radiation Facility, BP220, F-38043 Grenoble, France**

[2]*Technical University Berlin, Hardenbergstr. 36, D-10623 Berlin, Germany*

[3]*Helmholtz-Centre Berlin for Materials and Energy, Hahn-Meitner-Platz 1, D-14109 Berlin, Germany*

[4]*Institute for Photon Science and Synchrotron Radiation / ANKA, Karlsruhe Institute of Technology, PO Box 3640, D-76021 Karlsruhe, Germany*

[5]*Department of Metallurgical and Materials Engineering, Indian Institute of Technology Madras, Chennai 600036, India*

[6]*Charité, Campus Virchow Clinic, 13353 Berlin, Germany*

Pushing synchrotron X-ray radiography to increasingly higher image acquisition rates (currently up to 100 000 fps) while maintaining spatial resolutions in the micrometer range implies drastically reduced fields of view. As a consequence, either imaging a small sub-region of the sample with high spatial resolution or only the complete specimen with moderate resolution is applicable. We introduce a concept to overcome this limitation by making use of a semi-transparent X-ray detector positioned close to the investigated sample. The hard X-rays that pass through the sample either create an image on the first detector or keep on propagating until they are captured by a second X-ray detector located further downstream. In this way, a process can be imaged simultaneously in a hierarchical manner within a single exposure and a projection of the complete object with moderate resolution as well as a sub-region with high resolution are obtained. As a proof-of-concept experiment, image sequences of an evolving liquid metal foam are shown, employing frame rates of 1 000 images/s (1.2 µm pixel size) and 15 000 images/s (18.1 µm pixel size) for the first and second detector, respectively.



*OCIS codes:* 000.2170, 110.6915, 320.3980, 340.6720, 340.7440.

*Corresponding author: arack@snafu.de

## 1. Introduction

The development of hard X-ray imaging with high spatial resolution using indirect detection schemes (i. e. making use of visible light detection after x-ray conversion) reaches back to the 1970s when the first systems were constructed in order to perform so-called live topography, i. e. in-situ studies of crystal growth by means of diffraction imaging [1]. Indirect X-ray detectors frequently consist of a scintillator screen which converts X-rays into visible light photons which are then registered by a camera using fibre or microscopy optics. Indirect detectors are especially suitable for hard X-ray microimaging, they consist of components which are widely commercially available and they allow to reach micrometer spatial resolution while radiation resistent configurations are available [2], [3], [4], [5], [6], [7].

Besides applications for synchrotron-based microtomography, indirect detectors are successfully used for high-speed radioscopy, i. e. radiography with a time-resolution up to the microsecond range [8], [9]. Especially in combination with X-ray phase contrast, outstanding data acquisition rates can be reached [10], [11], [12], [13], [14]. Typically, X-ray inline phase contrast is employed due to its rather simple and robust concept: by leaving a propagation space between the sample and the imaging detector, interfaces within the probed specimen can be visualized due to the refraction at interfaces within the object [15], [16], [17], [18]. Other phase-sensitive imaging techniques such as grating-based interferometry have been used for fast imaging as well [19]. The choice of the propagation distance for inline phase contrast imaging is crucial especially when phase-retrieval techniques need to be applied [20], [21]. For high-speed radioscopy larger distances can be desirable in order to maximize the contrast while not reaching the far-field region [22].

Frequently, indirect detectors for fast hard X-ray radioscopy consist of a single-crystal scintillator (e. g., Ce-doped $Y_3Al_5O_{12}$ (YAG:Ce) or Ce-doped $Lu_3Al_5O_{12}$ (LuAG:Ce) [8]) which converts the X-ray photons into visible light. A mirror placed behind the scintillator screen at $45^o$ angle requires a long-working distance objective to project the luminescence image of the scintillator onto the sensor of a camera. This right-angle or periscope-like design allows one to keep the electronics and optical elements out of the intense beam, cf. the inset Fig. 1. Furthermore, protective lead glass can be applied in order to prevent the visible light objectives from darkening by the hard X-rays (care has to be taken to chose a type of lead glass which is not sensitive to the creation of color centers under hard X-ray illumination as well). Concerning the detector's field of view, one can consider the following

quantitative example: among the fastest cameras currently on the market the Photron SA5 (Photron Inc., USA) is considered. With a 1024 × 1024 CMOS sensor the camera can reach for up to 7 000 images/s without restricting the field-of-view (FOV). To reach for 50 000 images/s, a region-of-interest (ROI) of 512 × 272 pixels has to be adopted [23]. For a highly resolved radiographic projection image with a common pixel size between 1 µm and 2 µm, the FOV would be maximal 2 mm × 2 mm and can be as small as 0.5 mm × 0.3 mm. An example for an image sequence depicting a sub-region of a sample, taken in this case with 105 000 images/s acquisition rate (ROI of 233 × 163 pixels, 18.1 µm pixel size, 4.2 mm × 3.0 mm FOV) is shown in Fig. 2.

Frequently, high spatial resolution is required to study fine details in a sub-region of a specimen combined with the need of imaging the complete sample as well. In order to allow for such hierarchical studies a dual-detector concept is introduced in this article. It allows for taking radiographic projection images with high and moderate resolution simultaneously, i. e. a two-level approach which can easily be extended to further levels with additional detectors.

We demonstrate the potential of this two-level approach by the example of monitoring metal foaming processes. One needs to visualize the evolution of the entire foam [24, 25] and to determine parameters describing the global dynamics [26, 27]. Imaging of decay mechanisms like bursts of cell walls (leading to bubble coalescence) with a large FOV permits tracking of correlated phenomena such as rearrangements, avalanches or cascades [28] on a large sub-volume (or the entire specimen cross section). Focusing on smaller ROIs enables visualizing the disappearing cell walls in greater detail (an example is again the image sequence shown in Fig. 2). The aim of such experiments is to determine the destabilization mechanisms of such foams [27] and to measure the cell wall rupture time to find out the dependence of this time on the bubble geometry, thereby gaining knowledge about the effective viscosity of these complex liquids.

## 2. Instrumentation

The experiments were carried out at beamline ID19 of the European Synchrotron Radiation Facility in France [29]. The arrangement is briefly outlined in Fig. 1: a wiggler insertion device is used in order to generate the required high photon flux density. Approximately 150 m downstream of the source a furnace is placed which allows for metal foaming experiments under varying pressure [30]. Downstream of the furnace two detectors are positioned

at 5.2 m and 8.8 m distance, respectively.

The photon flux density emitted by the wiggler insertion device was chosen such that the heat load to the scintillator screens was not significantly affecting their light output, i. e. their conversion efficiency for X-rays to visible light photons (several scintillating materials show a decrease in light output with increasing temperature [8]). The spectrum for the corresponding insertion device gap of 52 mm (filtered with 1 mm aluminium) is plotted in Fig. 3 (calculated with Xop [32]): mean energy of around 34 keV, $2 \times 10^{13}$ photons/mm$^2$/s integral photon flux density and an energy spread of approximately of 90% (the absorption of the sample and the furnace housing are negligible at the dominating wavelengths used).

The first detector (microscope) at 5.2 m distance to the sample is operated in a semi-transparent manner: a 20-µm thick GGG:Eu single-crystal scintillator (Eu-doped $Gd_3Ga_5O_{12}$ grown on top of a 150-µm thick undoped GGG substrate [33]) converts the hard X-rays into visible light. The resulting luminescence image is projected via a mirror onto the chip of the CMOS-based camera pco.dimax (PCO AG, Germany, 2016 × 2016 pixel, 11 µm pixel size, 1279 full-frames per second (fps) maximum image acquisition rate [34]) by a Mitutoyo long-working distance objective (nominal 10× magnification, 0.28 numerical aperture). Thus, the detector operates with an effective pixel size of 1.2 µm and a 2.4 mm × 2.4 mm FOV. The choice of the objective was driven by the need to reach the highest spatial resolution possible, i. e., the 10× Mitutoyo is currently the objective with the largest magnification which can be used with the semi-transparent detector [5]. Images were acquired with 1 000 fps acquisition rate. Downstream of the scintillator only the glass mirror (1 mm thick, $45^o$ angle) as well as the housing of the microscope head made of 1-mm-thin vitreous carbon interacted with the beam, leading to an overall transmission of 34% at the mean energy of 34 keV. An integral amount of $2 \times 10^{12}$ photons/mm$^2$/s is absorbed by the 20-µm thick GGG:Eu active layer of the detector's scintillator screen (i. e. $3 \times 10^3$ photons per pixel within a single exposure). According to Fig. 3, the effective energy seen by the microscope detector is about 24 keV. $8 \times 10^{12}$ photons/mm$^2$/s are transmitted by the detector and the rest of the photons are absorbed by the substrate of the scintillator as well as the glass mirror (all calculated with Xop [32]). As a rough estimate based on the NA of the front objective, the refractive index of GGG:Eu and the camera characteristics, seven absorbed X-ray photons of the mean energy of 24 keV are required to give rise to one count in a pixel of the pco.dimax. Further characteristics on this semi-transparent detector

design have been published elsewhere [5].

At a distance of 8.8 m downstream of the furnace a second detector (macroscope) is placed that has been optimized for low magnifications [2]. The system consists of a 300-µm thick bulk YAG:Ce single-crystal scintillator. Similar like the semi-transparent detector its luminescence picture is projected via a mirror onto the CMOS chip of a Photron SA5 camera (1024 × 1024 pixel, 20 µm pixel size, 7 000 full-frames per second maximum image acquisition rate [23]) by a commercial tele-objective (type Zeiss Makro-Planar 100 mm/2.8, i. e. an NA of approximately 0.17). The measured effective pixel size of the detector is 18.1 µm. Images were acquired with 15 000 fps acquisition rate (by adopting a ROI of 432 × 305 pixel in order to reach the desired frame rate, i. e. a FOV of 7.8 mm × 5.5 mm). Here, the pixel size was chosen large enough in order to be able to image the complete specimen at a high frame rate. From the photons transmitted by the sample and the first detector, approximately $2.7 \times 10^{12}$ photons/mm$^2$/s are absorbed by the YAG:Ce scintillator screen (i. e. $5.9 \times 10^4$ photons per pixel within a single exposure (calculated with Xop [32]), neither the analog-digital conversion factor of the camera nor the wavelength response is available). The effective energy seen by the macroscope detector is about 36 keV. No synchronization between the two image acquisition systems was carried out.

Considering the huge difference in pixel size, the two detectors operate in different phase contrast regimes. The macroscope with 18.1 µm pixel size records images in the edge enhancement regime, the first Fresnel zone ($\sqrt{\lambda z} \approx 18$ µm, with $\lambda$: the (mean) wavelength seen by the detector and $z$: the propagation distance) being comparable the pixel size. The microscope with 1.2 µm pixel size records images in a more holographic regime, the first Fresnel zone of 16 µm being significantly larger than the pixel size. Considering the spatial features present in the sample, the image still closely resembles a faithfull projection of the object. In practice, the distance of the macroscope has been set to the maximum achievable one in order to optimize the general image contrast. The distance of the microscope has been chosen to emphasize the contrast on the cell wall thickness which is on the order of tens of micrometers [25].

## 3. Hierarchical single-shot radioscopy

In Fig. 4 (left) overview images acquired with the macroscope 8.8 m downstream of the experiment are shown (15 000 fps). A coalescence event between two pores is depicted. To

allow distinguishing features which are generally much more clearly visible in the moving image, the right column displays the silhouette of the main event. A difference image is placed at the bottom of the figure. The full movie is accessible via the online material (cf. supplementary material, movie 917310.avi). Image artifacts due to an imperfect flat-field correction are visible as the rectangular frame near the border (related to the fact that moving the semi-transparent detector out for acquiring the flat-field images changes the heat load to the macroscope). The contrast exploited is widely dominated by diffraction/refraction, related to the large propagation distance used as well as the low absorption of the aluminium specimen at the dominating energy. Wavefront distortions introduced by the semi-transparent detector can be neglected due to the large pixel size applied.

The advantages of performing hierarchical radiography in a single shot are illustrated in Fig. 5: on the left side, the same time series as displayed in Fig. 4 is shown. Again, the contrast exploited is dominated by refraction rather than absorption. The red box marks a region where one can zoom in thanks to the high-resolution pictures acquired with the semi-transparent detector 5.2 m downstream of the experiment. The arrows indicate details barely resolved in the overview images. One can, for instance, determine the maximal cell wall thickness just before rupture (here $<$60 µm) and compare it with the literature [25], [35]. The complete picture on the left side gives insight into local re-arrangements taking place while two of the lamellae disappear. In order to get a more realistic impression of the dynamics captured the reader is kindly referred to the high-resolution movie available online (binning 4 $\times$ 4 was applied to reduce the size, cf. supplementary material, movie 917311.avi).

This example of a coalescence event imaged simultaneously at high and medium spatial resolution allows one to track on the macroscopic scale if for example the event is isolated or part of a cascade of coalescence events, i. e. it allows us to reveal the big picture. In contrast, the high-resolution images tell us on how the cell wall ruptures introduce topological re-arrangements in the local pore environment.

## 4. Summary & Outlook

A concept to acquire several hierarchical radioscopic projection images of the very same temporal event in a single shot has been successfully demonstrated. The backbone of the experiment is a semi-transparent detector which transmits enough radiation to operate other

detectors further downstream. The performance of the semi-transparent detector could be significantly improved in the future by deploying thin free-standing single-crystal scintillators, i. e. without a substrate (such as LuAG:Ce by Crytur, Czech Republic) which would reduce parasitic absorption of the semi-transparent detector and hence, allow for a higher photon flux density on the detector further downstream [36]. Mirrors made of carbon rather than glass could further reduce scattering as well as X-ray fluorescence. Such secondary radiation can darken objectives as well as deteriorate the spatial resolution of the imaging system by creating parasitic luminescence in the scintillator screen. After the optimization mentioned, in principle more than two detectors could be operated inline, depending as well on the photon energy used. By combining detectors at different propagation distances, more sophisticated contrast mechanisms such as holotomography could become available in a single shot [37]. This technique is currently employed at beamline ID22NI of the ESRF [38] as well as the Tomcat beamline of the Swiss Light Source [39]. Here, more care needs to be taken with the selection of the propagation distances applied [21]. In addition, synchronization of the different cameras used needs to be considered for the future in order to directly correlate pictures acquired by the different detectors.

**Acknowledgments**

Marco Di Michiel and Mario Scheel (both ESRF) for borrowing the macroscope optical system, the VKT GmbH, Germany for providing the Photron SA5 as well as Jean-Paul Valade (ESRF) for general support during the experiment. The anonymous reviewers for their comments which substantially improved the quality of our manuscript.

**References**

1. W. Hartmann, G. Markewitz, U. Rettenmaier, and H. J. Queisser, "High resolution direct-display X-ray topography," Appl. Phys. Lett. **27**, 308–309 (1975).
2. A. Koch, "Lens coupled scintillating screen-CCD X-ray area detector with a high quantum efficiency," Nucl. Instrum. & Meth. in Phys. Res. A **348**, 654–658 (1994).
3. U. Bonse and F. Busch, "X-ray computed microtomography ($\mu$CT) using synchrotron radiation (SR)," Prog. Biophys. Molec. Biol. **65**, 133–169 (1996).
4. A. Koch, C. Raven, P. Spanne, and A. Snigirev, "X-ray imaging with submicrometer resolution employing transparent luminescent screens," J. Opt. Soc. Am. A **15**, 1940–1951 (1998).

5. P. Douissard, A. Cecilia, X. Rochet, X. Chapel, T. Martin, T. van de Kamp, L. Helfen, T. Baumbach, L. Luquot, X. Xiao, J. Meinhardt, and A. Rack, "A versatile indirect detector design for hard X-ray microimaging," J. Instrum. **9**, P09016 (2012).
6. A. N. Danilewsky, A. Rack, J. Wittge, T. Weitkamp, R. Simon, H. Riesemeier, and T. Baumbach, "White beam synchrotron topography using a high resolution digital X-ray imaging detector," Nucl. Instrum. & Meth. in Phys. Res. B **266**, 2035–2040 (2008).
7. A. Rack, S. Zabler, B. R. Müller, H. Riesemeier, G. Weidemann, A. Lange, J. Goebbels, M. Hentschel, and W. Görner, "High resolution synchrotron-based radiography and tomography using hard X-rays at the BAMline (BESSY II)," Nucl. Instr. & Meth. in Phys. Res. A **586**, 327–344 (2008).
8. M. Di Michiel, J. M. Merino, D. Fernandez-Carreiras, T. Buslaps, V. Honkimäki, P. Falus, T. Martins, and O. Svensson, "Fast microtomography using high energy synchrotron radiation," Rev. Sci. Instrum. **76**, 043702–1–7 (2005).
9. F. García-Moreno, A. Rack, L. Helfen, T. Baumbach, S. Zabler, N. Babcsán, J. Banhart, T. Martin, C. Ponchut, and M. Di Michiel, "Fast processes in liquid metal foams investigated by high-speed synchrotron X-ray microradioscopy," Appl. Phys. Lett. **92**, 134104–1–3 (2008).
10. J. Wang, "Ultrafast X-ray imaging of fuel sprays," in "AIP Conf. Proc. (SRI06)," , vol. 879, J.-Y. Choi and S. Rah, eds. (2007), vol. 879, pp. 1535–1538.
11. Y. Wang, X. Liu, K.-S. Im, W.-K. Lee, J. Wang, K. Fezzaa, D. L. S. Hung, and J. R. Winkelman, "Ultrafast X-ray study of dense-liquid-jet flow dynamics using structure-tracking velocimetry," Nat. Phys. **4**, 305–309 (2008).
12. A. Rack, F. García-Moreno, T. Baumbach, and J. Banhart, "Synchrotron-based radioscopy employing spatio-temporal micro-resolution for studying fast phenomena in liquid metal foams," J. Synchrotron Radiat. **16**, 432–434 (2009).
13. A. Rack, F. García-Moreno, C. Schmitt, O. Betz, A. Cecilia, A. Ershov, T. Rack, J. Banhart, and S. Zabler, "On the possibilities of hard X-ray imaging with high spatio-temporal resolution using polychromatic synchrotron radiation," J. X-Ray Sci. Tech. **18**, 429–441 (2010).
14. K.-C. Lin, C. Rajnicek, J. McCall, C. Carter, and K. Fezzaa, "Investigation of pure- and aerated-liquid jets using ultra-fast X-ray phase contrast imaging," Nucl. Instrum.

& Meth. in Phys. Res. A **649**, 194–196 (2011).

15. A. Snigirev, I. Snigireva, V. Kohn, and S. Kuznetsov, "On the possibilities of X-ray phase contrast microimaging by coherent high-energy synchrotron radiation," Rev. Sci. Instrum. **66**, 5486–5492 (1995).
16. P. Cloetens, R. Barrett, J. Baruchel, J.-P. Guigay, and M. Schlenker, "Phase objects in synchrotron radiation hard X-ray imaging," J. Phys. D: Appl. Phys. **29**, 133–146 (1996).
17. S. W. Wilkins, T. E. Gureyev, D. Gao, A. Pogany, and A. W. Stevenson, "Phase-contrast imaging using polychromatic hard X-rays," Nature **384**, 335–337 (1996).
18. K. A. Nugent, T. E. Gureyev, D. F. Cookson, D. Paganin, and Z. Barnea, "Quantitative phase imaging using hard X rays," Phys. Rev. Lett. **77**, 2961–2964 (1996).
19. A. Momose, W. Yashiro, H. Maikusa, and Y. Takeda, "High-speed X-ray phase imaging and X-ray phase tomography with Talbot interferometer and white synchrotron radiation," Opt. Express **17**, 12540–12545 (2009).
20. D. Paganin, S. C. Mayo, T. E. Gureyev, P. R. Miller, and S. W. Wilkins, "Simultaneous phase and amplitude extraction from a single defocused image of a homogeneous object," J. Microsc.–Oxford **206**, 33–40 (2002).
21. S. Zabler, P. Cloetens, J.-P. Guigay, J. Baruchel, and M. Schlenker, "Optimization of phase contrast imaging using hard X rays," Rev. Sci. Instrum. **76**, 073705 (2005).
22. V. G. Kohn, T. S. Argunova, and J. H. Je, "Far-field X-ray phase contrast imaging has no detailed information on the object," J. Phys. D: Appl. Phys. **43**, 442002 (2010).
23. Photron USA, Inc., *FASTCAM SA5 Data Sheet*, http://www.photron.com (accessed August 2013).
24. H. Stanzick, M. Wichmann, J. Weise, L. Helfen, T. Baumbach, and J. Banhart, "Real-time X-ray investigation of aluminium foam sandwich production," Adv. Eng. Mater. **3**, 407 (2001).
25. H. Stanzick, M. Wichmann, J. Weise, L. Helfen, T. Baumbach, and J. Banhart, "Process control in aluminium foam production using real-time X-ray radioscopy," Adv. Eng. Mater. **4**, 814–823 (2002).
26. R. Verdejo, F.J. Tapiador, L. Helfen, M.M. Bernal, N. Bitinis, and M.A. Lopez-Manchado, "Fluid dynamics of evolving foams," Phys. Chem. Chem. Phys. **11**, 10860–10866 (2009).

27. A. Myagotin, L. Helfen, and T. Baumbach, "Quantitative coalescence measurements for foaming metals by in situ radiography," Scripta Mater. **67**, 775–778 (2012).
28. L. Helfen, H. Stanzick, J. Ohser, K. Schladitz, P. Pernot, J. Banhart, and T. Baumbach, "Investigation of the foaming process of metals by synchrotron-radiation imaging," in "Proc. of SPIE," vol. 5045, N. Meyendorf, G. Baaklini, and B. Michel, eds. (2003), pp. 254–265.
29. T. Weitkamp, P. Tafforeau, E. Boller, P. Cloetens, J.-P. Valade, P. Bernard, F. Peyrin, W. Ludwig, L. Helfen, and J. Baruchel, "Status and evolution of the ESRF beamline ID19," in "AIP Conf. Proc. (ICXOM20)," vol. 1221, M. Denecke and C. T. Walker, eds. (2010), pp. 33–38.
30. F. Garcia-Moreno, N. Babcsan, and J. Banhart, "X-ray radioscopy of liquid metal-foams: influence of heating profile, atmosphere and pressure," Colloids Surf. A **263**, 290–294 (2005).
31. P. Cloetens, W. Ludwig, E. Boller, L. Helfen, L. Salvo, R. Mache, and M. Schlenker, "Quantitative phase contrast tomography using coherent synchrotron radiation," in "Proc. of SPIE: Development in X-Ray Tomography III," U. Bonse, ed. (2002), vol. 4503, pp. 82–91.
32. M. S. del Río and R. J. Dejus, "Xop 2.1 — a new version of the X-ray optics software toolkit," AIP Conference Proc. (SRI2003) **705**, 784–787 (2004).
33. T. Martin and A. Koch, "Recent developments in X-ray imaging with micrometer spatial resolution," J. Synchrotron Rad. **13**, 180–194 (2006).
34. PCO AG, *pco.dimax Data Sheet*, http://www.pco.de (accessed August 2013).
35. A. Myagotin, A. Ershov, L. Helfen, R. Verdejo, A. Belyaev, and T. Baumbach, "Coalescence analysis for evolving foams *via* optical flow computation on projection image sequences," J. Synchrotron Rad. **19**, 483–491 (2012).
36. CRYTUR, spol. s r.o., http://www.crytur.cz (accessed August 2013).
37. P. Cloetens, W. Ludwig, J. Baruchel, D. V. Dyck, J. Landuyt, J. P. Guigay, and M. Schlenker, "Holotomography: Quantitative phase tomography with micrometer resolution using hard synchrotron radiation X-rays," Appl. Phys. Lett. **75**, 2912–2914 (1999).
38. G. Martínez-Criado, R. Tucoulou, P. Cloetens, P. Bleuet, S. Bohic, J. Cauzid, I. Kieffer, E. Kosior, S. Labouré, S. Petitgirard, A. Rack, J. A. Sans, J. Segura-Ruiz, H. Suhonen,

J. Susini, and J. Villanova, "Status of the hard X-ray microprobe beamline ID22 of the European Synchrotron Radiation Facility," J. Synchrotron Radiat. **19**, 10–18 (2012).

39. R. Mokso, F. Marone, S. Irvine, M. Nyvlt, D. Schwyn, K. Mader, G. K. Taylor, H. G. Krapp, M. Skeren, and M. Stampanoni, "Advantages of phase retrieval for fast X-ray tomographic microscopy," J. Phys. D: Appl. Phys. **46**, in press (2013).
40. F. Garcia-Moreno, M. Mukherjee, C. Jimenez, A. Rack, and J. Banhart, "Metal foaming investigated by X-ray radioscopy," Metals **2**, 10–21 (2012).

**List of Figure Captions**

Fig. 1. Outline of the experiment: the wiggler insertion device emits a broad energy spectrum filtered by absorbers, 150 m downstream the experiment is placed. At a distance of 5.2 m from the experiment a semi-transparent high-resolution detector is positioned (10× Mitutoyo objective with NA=0.28, 1.2 µm effective pixel size), approximately 3.6 m further downstream a macroscope detector with 18.1 µm effective pixel size. Both systems are equipped with fast CMOS cameras for high data acquisition rates (the common lead shielding required to protect the camera electronics from scattered radiation has been removed for the photos). The inset shows the common design of a radiation resistent indirect X-ray image detector.

Fig. 2. Coalescence event in a liquid aluminium foam (AlSi6Cu4 with 0.6 wt-% $TiH_2$ at a temperature of 640°C) captured with an acquisition rate of 105 000 images/s (9.5 µs temporal sampling / 6 µs exposure time, 8 m propagation distance, 18.1 µm effective pixel size, approximately 4.2 mm × 3.0 mm FOV) [40]. Times given refer to the first frame.

Fig. 3. Plot of the different effective photon energy spectra as i) transmitted by the sample, ii) absorbed by the 20-µm thick active layer GGG:Eu of the first, semi-transparent detector, iii) transmitted by the first detector, iv) absorbed by the 300-µm thick YAG:Ce single-crystal scintillator of the second detector (calculated with Xop [32]). The second detector is not transparent, i. e. its transmission is zero.

Fig. 4. Overview images acquired with the medium-resolution detector 8.8 m downstream of the experiment. Left: the coalescence of two cells is captured with an image acquisition rate of 15 000 fps (artifacts from imperfect flat-field correction remain). Right: the silhouette of the event. The picture at the bottom is the difference between the first and the last frame. In order to fully exploit the dynamics of the event captured the reader is kindly referred to the complete movie available online (cf. supplementary material, movie 917310.avi). See furthermore Fig. 5.

Fig. 5. Hierarchical radiography performed in a single shot: the left column shows the same time series as Fig. 4, the red box marks the region one can zoom in with the pictures taken with the semi-transparent high-resolution detector 5.2 m downstream of the experiment (depicted on the right, contrast inverted for better visibility). The arrows mark

a part of the event barely resolved in the overview images. The high-resolution images acquired with 1 000 fps allow one to have a detailed view of the re-arrangements taking place during coalescence. The corresponding movie is available online and the reader is kindly referred to it in order to explore the dynamics captured with the high-resolution movie (cf. supplementary material, movie 917311.avi).

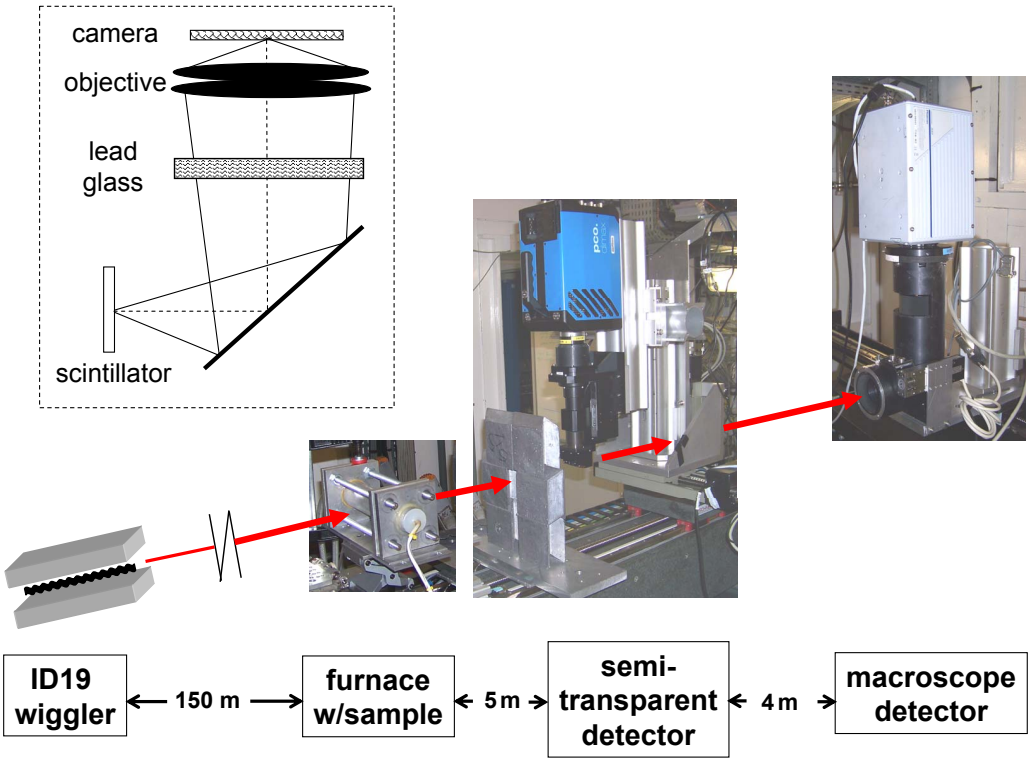


Fig. 1. (color-online only) Outline of the experiment: the wiggler insertion device emits a broad energy spectrum filtered by absorbers, 150 m downstream the experiment is placed. At a distance of 5.2 m from the experiment a semi-transparent high-resolution detector is positioned (10× Mitutoyo objective with NA=0.28, 1.2 µm effective pixel size), approximately 3.6 m further downstream a macroscope detector with 18.1 µm effective pixel size. Both systems are equipped with fast CMOS cameras for high data acquisition rates (the common lead shielding required to protect the camera electronics from scattered radiation has been removed for the photos). The inset shows the common design of a radiation resistent indirect X-ray image detector.

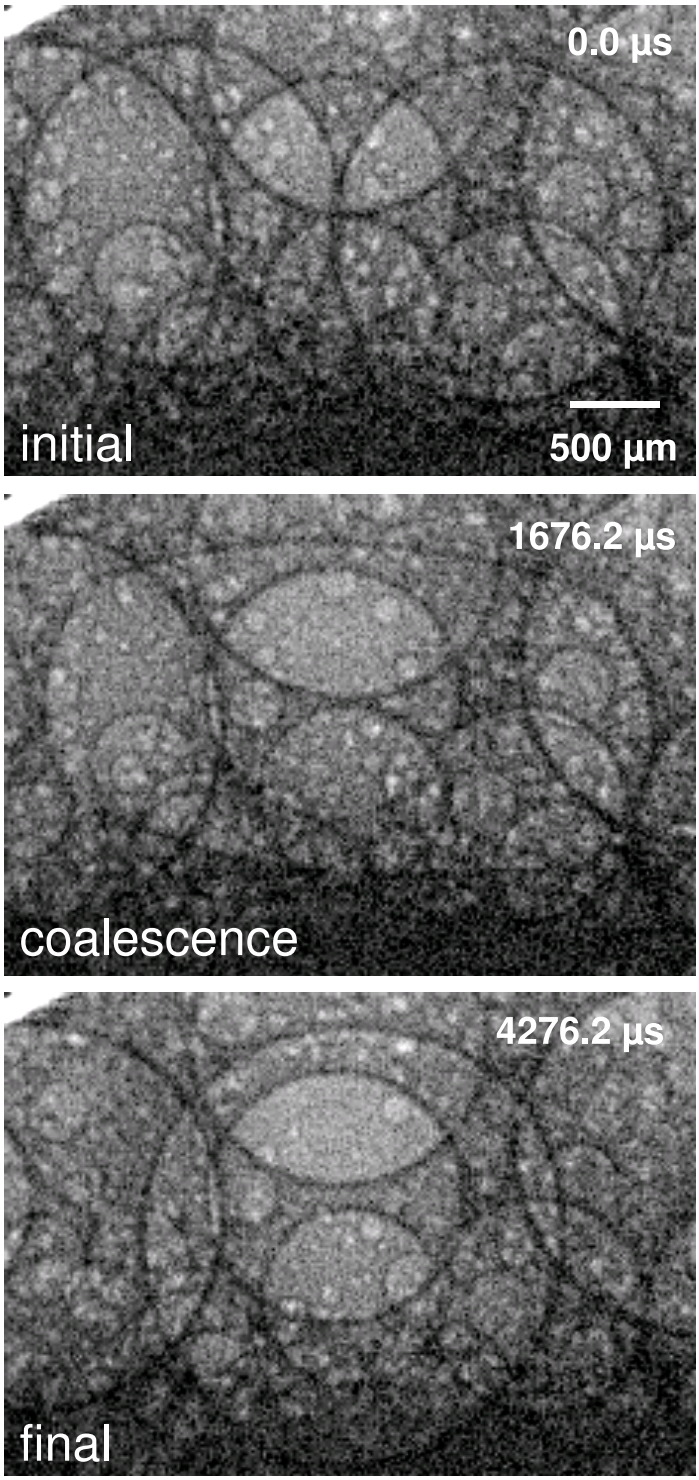


Fig. 2. Coalescence event in a liquid aluminium foam (AlSi6Cu4 with 0.6 wt-% $TiH_2$ at a temperature of 640°C) captured with an acquisition rate of 105 000 images/s (9.5 µs temporal sampling / 6 µs exposure time, 8 m propagation distance, 18.1 µm effective pixel size, approximately 4.2 mm × 3.0 mm FOV) [40]. Times given refer to the first frame.

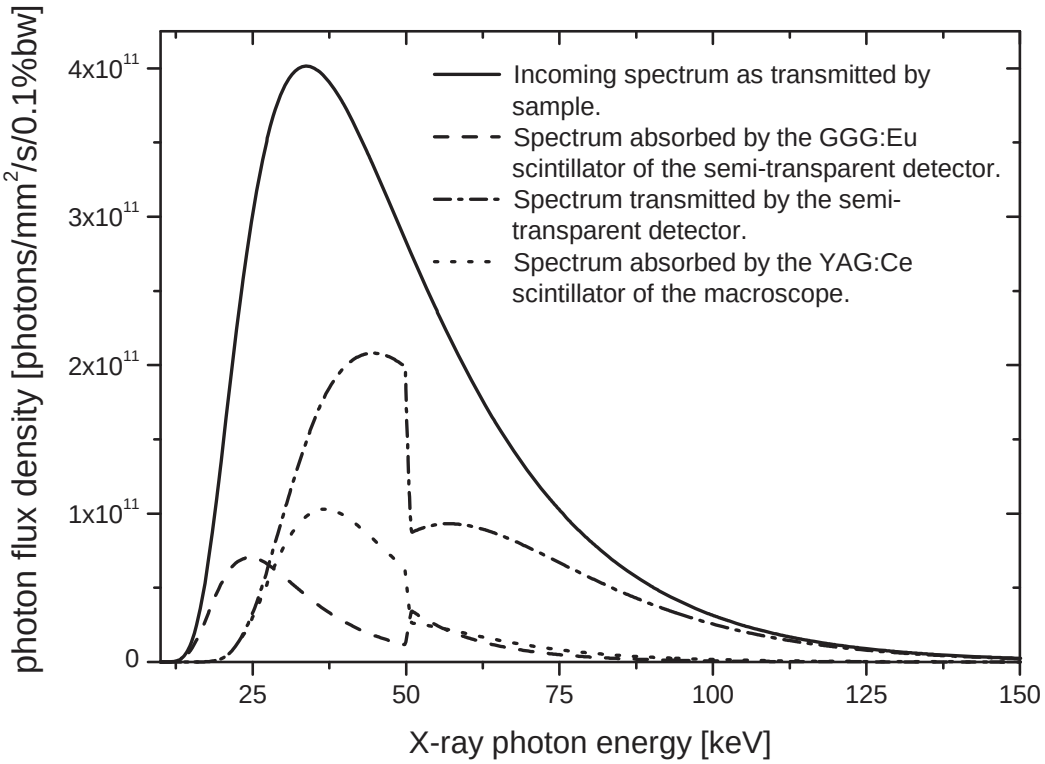


Fig. 3. Plot of the different effective photon energy spectra as i) transmitted by the sample, ii) absorbed by the 20-µm thick active layer GGG:Eu of the first, semi-transparent detector, iii) transmitted by the first detector, iv) absorbed by the 300-µm thick YAG:Ce single-crystal scintillator of the second detector (calculated with Xop [32]). The second detector is not transparent, i. e. its transmission is zero.

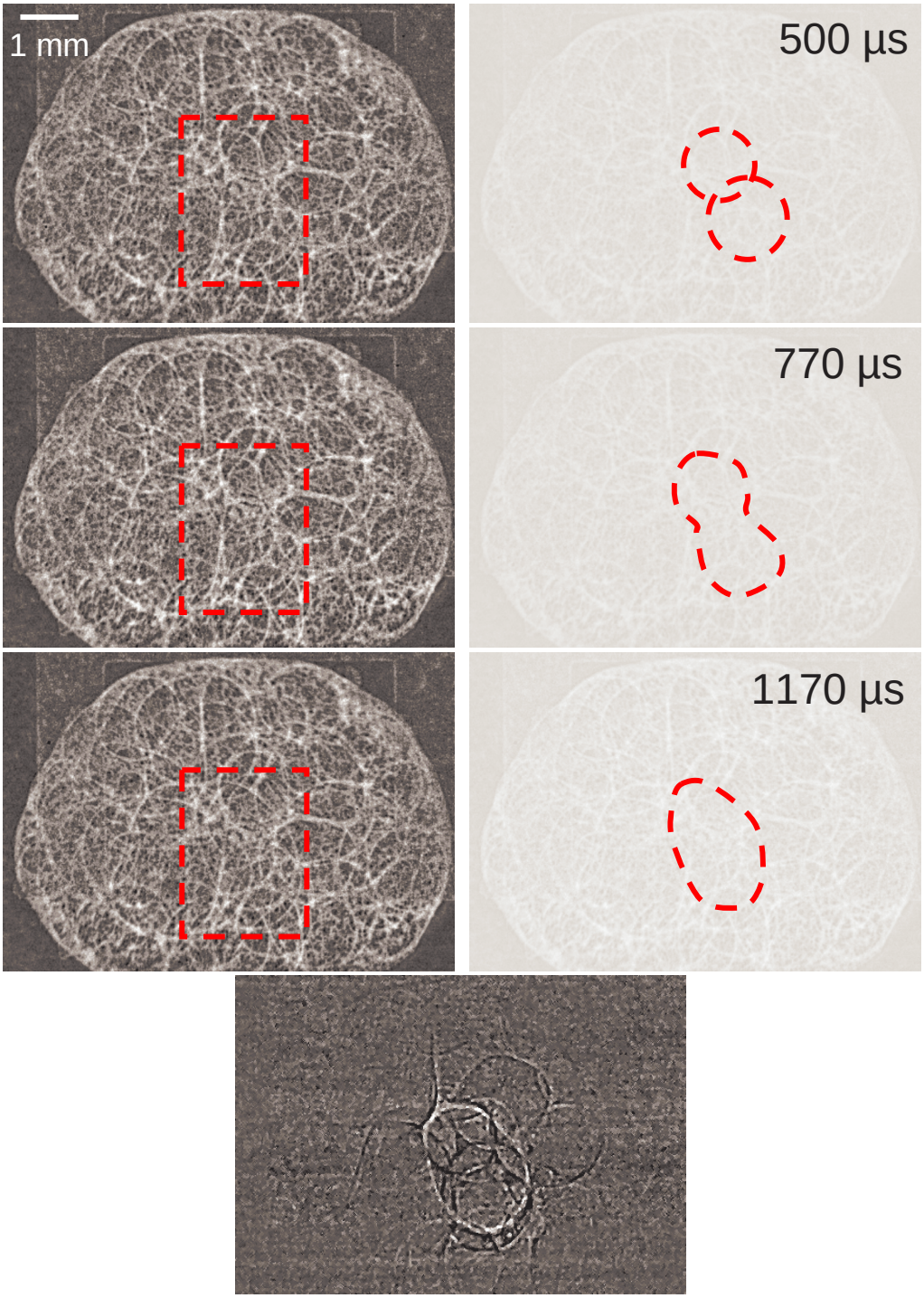


Fig. 4. (color-online only) Overview images acquired with the medium-resolution detector 8.8 m downstream of the experiment. Left: the coalescence of two cells is captured with an image acquisition rate of 15 000 fps (artifacts from imperfect flat-field correction remain). Right: the silhouette of the event. The picture at the bottom is the difference between the first and the last frame. In order to fully exploit the dynamics of the event captured the reader is kindly referred to the complete movie available online (cf. supplementary material, movie 917310.avi). See furthermore Fig. 5.

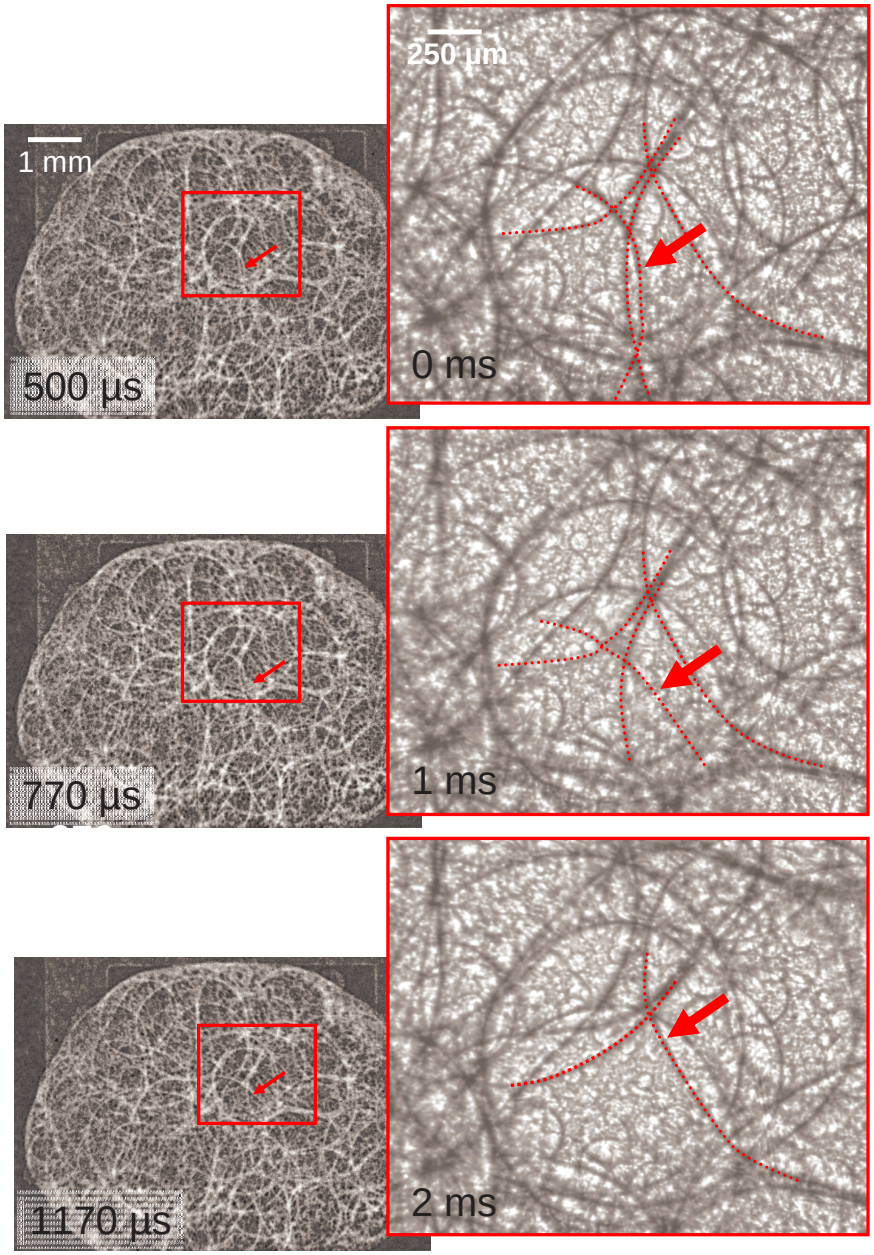


Fig. 5. (color-online only) Hierarchical radiography performed in a single shot: the left column shows the same time series as Fig. 4, the red box marks the region one can zoom in with the pictures taken with the semi-transparent high-resolution detector 5.2 m downstream of the experiment (depicted on the right, contrast inverted for better visibility). The arrows mark a part of the event barely resolved in the overview images. The high-resolution images acquired with 1 000 fps allow one to have a detailed view of the re-arrangements taking place during coalescence. The corresponding movie is available online and the reader is kindly referred to it in order to explore the dynamics captured with the high-resolution movie (cf. supplementary material, movie 917311.avi).